Limitations of decomposition-based imaging of longitudinal absorber configurations

S. D. Campbell, S. D. Grobe, I. L. Goodin, Q. Su, and R. Grobe
Intense Laser Physics Theory Unit and Department of Physics, Illinois State University, Normal, Illinois 61790-4560, USA
(Received 26 October 2007; published 20 February 2008)

We examine theoretically and experimentally an imaging scheme that uses the transverse intensity profile of the scattered light to reconstruct the locations of absorbers embedded in a turbid medium. This method is based on an *a priori* knowledge of the scattered light patterns associated with a single absorber that is located at various positions inside the medium. We discuss the range of validity of this method, and its sensitivity with regard to noise, and propose an algorithm to improve its accuracy.

DOI: 10.1103/PhysRevA.77.023821 PACS number(s): 42.25.Dd, 42.30.Lr

I. INTRODUCTION

In the past decade great progress has been reported for using the properties of the scattered waves to reconstruct the space dependent properties of materials [1–9]. Applications include a wide range of studies from stellar atmospheres in astrophysics [10], identification of certain geological layers in seismology [11], new ways to see through murky water in oceanography [12], identifying the health of plant canopies in environmental science [13], to recovering cancerous tumors in bio-optical medicine [6–9]. In most of these applications the forward problem of finding the properties of the scattered wave for a material with a given spatially dependent scattering or absorption is nontrivial and usually requires approximations. The associated inverse procedure of reconstructing the medium's characteristics from the scattered wave is typically even more difficult, sometimes resulting in ill-posed problems that should be avoided [14].

In many imaging situations, the theoretical description is based on the inversion of the Fredholm equation of the first kind [15,16]. This type of integral equation can be difficult to solve. For example, in bio-optical imaging the interaction between the light and a biological tissue is described by the Boltzmann equation. Here the optical properties of the tissue are described by scattering and absorption coefficients that depend on the position. The forward problem is typically approximated by the diffusion equation. If the scattered light associated with the spatial inhomogeneity is much weaker than the scattered light of the background, the Born approximation [17–22] can be applied resulting in a linear dependence between the scattering coefficient and the corresponding scattered light. The resulting Fredholm equation is then the starting point for various inversion algorithms. The typical goal in bio-optical imaging is to reconstruct the location of an embedded object without any prior knowledge about the scattering medium. However, some progress has been reported recently on how to include some prior knowledge obtained from other methods in order to improve the image reconstruction [23,24].

In this paper we will examine a less ambitious inversion scheme. It requires a certain *ab initio* knowledge of the scattered light for media that contain a single absorber at a known position. This scheme permits the reconstruction of the positions of entire groups of absorbers in regimes where the Born approximation could become invalid as the optical response is nonlinear. Once the medium is "mapped out" and the data bank of the scattered light patterns for all possible single-absorber images is archived, one can reconstruct the locations of an arbitrary set of objects. The combined image obtained from several absorbers can be decomposed approximately into the arithmetic sum of these individual single-absorber images with suitable weights that can be obtained from multiple regression analysis.

The paper follows up on a recent work that demonstrated a first proof of concept of decomposition based imaging (DBI). [25] It raised several challenges about the method's precise range of validity, its sensitivity to noise, possible generalizations to imaging of absorbers that are located outside the grid defined by the *a priori* calibration data, and about possible algorithms to improve the interpretation of the inversion data. In this work we will report on progress in each area. In Sec. II, we describe the downstream model that can provide us very efficiently with scattered light distribution for media with an arbitrary number of absorbers. In Sec. III we examine the quality of this approach by comparing the predicted distribution with experimental data for media with a single absorber. In Sec. IV we discuss the decomposition based imaging scheme, apply it to the experimental situation, and use the theoretically obtained data to examine its range of validity. In Sec. V we show how a simple algorithm can be applied to the raw data in order to improve the imaging scheme significantly. In Sec. VI we examine our inversion scheme for the more general situation in which an absorber is located at a position that has not been mapped out by the *a priori* calibration data. In the Sec. VII we conclude with a summary and outlook on further work.

II. DOWNSTREAM MODEL

The decomposition based imaging scheme (DBI) will be described in Sec. III. In contrast to many other imaging schemes, DBI assumes some prior knowledge about the medium's optical response. As a result of this limitation, this inversion scheme itself does not require a specific forward model. However, in order to examine systematically the range of validity of our imaging scheme for a wide range of parameters, we need to generate theoretically the scattered light patterns in an efficient and fully controlled way. These computations require a forward model.

As mentioned in the Introduction, the interaction of an electromagnetic field with a turbid medium is often described by the radiative transfer (Boltzmann) equation [1,2] for which the light distribution is modeled by the position $\mathbf{r}$ and $\mathbf{\Omega}$ dependent irradiance $I(\mathbf{r},\mathbf{\Omega})$. The medium is characterized by a spatially dependent scattering and absorption coefficient. Unfortunately, there are only a few analytical solutions to this equation available and often large scale Monte Carlo type computations are required, especially if there are inhomogeneities embedded in the highly scattering medium as in our situation.

To obtain the scattered light data in an efficient way, we have adopted a simple downstream model, in which the transverse brightness pattern of the light, denoted by $L(y,z)$, is evolved through the medium by the consecutive actions of scattering and absorber operators $\hat{S}$ and $\hat{A}$. The incoming laser beam enters our medium from the right at $z=0$. We assume its intensity in the transverse direction is represented by a Gaussian profile $L(y,z=0)=\exp[-(y/w_L)^2]$, where w_L denotes the transverse width of the beam and y is the distance from the z axis. In this work we have used $w_L=1.1$ mm, reflecting a typical width of our lasers. In the downstream model, the propagation of the light through a scattering layer of thickness D and an effective scattering strength δ_S is given by the integral

$$L(y,z+D)=\int dy' G_S(y-y',D,\delta_S)L(y',z)\equiv \hat{S}(D)L(y,z). \tag{2.1}$$

The propagation of the light profile through an absorber is represented by the multiplication

$$L(y,z+\varepsilon)=G_A(y,d,O_A)L(y,z)\equiv \hat{A}L(y,z), \tag{2.2}$$

where we have assumed the absorber has a negligible longitudinal extension ε. In the numerical example below, we represent the absorber by the "hole-burning" function $G_A(y,d,O_A)\equiv 1-O_A\exp[-(2y/d)^{20}]$. Here d denotes the diameter and O_A $(0\le O_A\le 1)$ models the opacity of the absorber. For the scattering kernel $G_S(y-y',D,\delta_S)$ we have examined Gaussian and Lorentzian distribution functions, $G_S(y,D,\delta_S')=[1/(\pi D\delta_S')]^{1/2}\exp[-y^2/(D\delta_S')]$ and $G_S(y,D,\delta_S)=D/[\pi\delta_S(D^2+\delta_S^{-2}y^2)]$, respectively. A comparison with experimental data (below) can suggest which of the two kernels is more suitable. Both kernels fulfill the required additivity property, $\hat{S}(D)\hat{S}(D)=\hat{S}(2D)$.

Let us now assume that there are four locations z_n with $n=1,\ldots,4$ at which we can place a rod shaped absorber into the medium. The geometry is sketched in Fig. 1. The four digit pattern $(ijkl)$ with $i,j,k,l=0$ or 1 denotes the occupation of the corresponding locations with rods. For example, the notation (1101) refers to a three-absorber configuration with rods that are located at positions z_4, z_3, and z_1. In order to use the downstream model to calculate the corresponding transverse light distribution at output $z=W$ for this configuration, we have to apply the actions of the scattering and absorption operators $\hat{S}$ and $\hat{A}$ consecutively to the initial light intensity profile $L(y,z=0)$. In technical terms, this corresponds to several consecutive integrations and multiplications according to

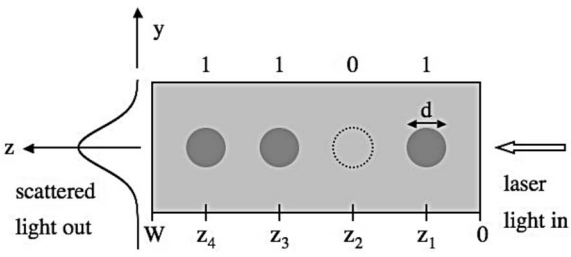

FIG. 1. Sketch of the experimental setup with three rods embedded into the tank.

$$L_{1101}(y,z=W)=\hat{S}(W-z_4)\hat{A}\hat{S}(z_4-z_3)\times\hat{A}\hat{S}(z_3-z_1)\hat{A}\hat{S}(z_1)L(y,z=0). \tag{2.3}$$

Here the rightmost operation $\hat{S}(z_1)$ represents the first scattering layer from the right edge of the medium at $z=0$ to the location of the first (rightmost) absorber at z_1.

As an example, we show in Fig. 2 how the brightness pattern evolves for the (1101) configuration. A very narrow incoming Gaussian profile (bottom graph) widens as it propagates through the first scattering layer of width z_1. The middle part of the resulting distribution is then removed due to the action of the absorption operator $\hat{A}$. The created hole of diameter d then widens and partially fills up as the profile is evolved to z_3 through the next scattering layer of width z_3-z_1. At z_3 the absorption operator inserts another hole into the distribution which is then scattered to z_4, hole-punched, and finally scattered to the left edge of the medium at $z=W$.

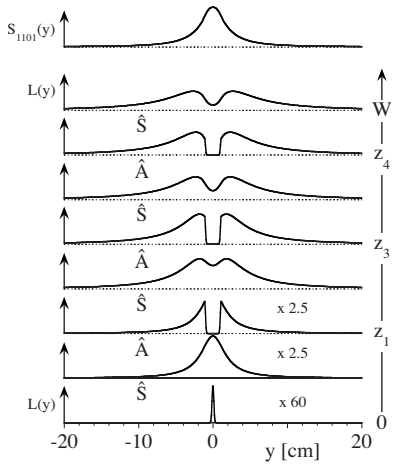

FIG. 2. Propagation of the transverse brightness profile $L(y)$ for the downstream model to generate the shadow pattern for the three-rod configuration (1101). The bottom shows the incoming laser beam with width $w_L=0.11$ cm. We used the Lorentzian scattering kernel with $\delta_S=0.53$, and the absorbers with $d=0.95$ cm and opacity $O_A=1$. The absorbers were placed at locations $z_1=6.5$ cm, $z_3=11.1$ cm, and $z_4=13.4$ cm, measured from the entry surface of the medium of total length $W=16$ cm.

In order to obtain the corresponding shadow pattern we have to subtract the scattered light pattern associated with no absorber, $L_{0000}(y,z=W)=\hat{S}(W)L(y,z=0)$, leading to

$$S_{ijkl}(y,z=W) \equiv L_{0000}(y,z=W) - L_{ijkl}(y,z=W). \quad (2.4)$$

The corresponding shadow pattern for $S_{1101}(y,z=W)$ is displayed by the top graph in Fig. 2.

A system with a maximum of four possible absorbers can have eleven different arrangements. This signal space includes six two-rod configurations (1100, 1010, 1001, 0110, 0101, and 0011), four three-rod configurations (1110, 1101, 1011, and 0111), and finally one four-rod configuration (1111). As we assume an *a priori* knowledge of the four single-rod configurations (1000, 0100, 0010, and 0001), we call them calibration states.

III. EXPERIMENTAL LIGHT SCATTERING DATA

The top view of the experimental setup was already sketched in Fig. 1. We have illuminated a 12 liter glass tank [30 cm×16 cm×26 cm] with a 661 nm diode laser with a power of 80 mW and input beam diameter of about w_L =1.1 mm. At locations z=6.5, 8.8, 11.1, and 13.4 cm from the entry surface of the tank we have placed cylinders as absorbers. These plastic rods have a diameter of d =0.95 cm and a length of 20.3 cm. As a scattering medium we used a 2% milk–water mixture with various concentrations. A 3.2 mm diameter optical fiber bundle connected to a broad area detector (NewFocus 2031) scanned the scattered light in 481 steps along the y direction, parallel to the exit wall of the tank.

In a separate work [26–28], we described how one can use measurements of the light distribution inside the medium along the optical axis to determine reliably the scattering and absorption coefficients as well as the anisotropy factor g. For a HeNe laser the empirical formula $\mu_s=\rho$ 310 cm^{-1} approximates the scattering coefficient, where ρ denotes the concentration of 2% milk in the water. For the data presented below we chose ρ=100 ml milk/9.2 l water suggesting a scattering coefficient of about μ_s=3.3 cm^{-1} leading to an inverse scattering length of about 0.3 cm. In other words, the rod spacings of either 2.3 cm, 4.6 cm, or 6.9 cm, are much larger than this length. With an isotropy of about g=0.93 this corresponds to a reduced scattering length of $[\mu_s']^{-1}$=4.2 cm.

In order to improve the accuracy, the data were averaged over two independent runs. In Fig. 3 the dashed curves show the four single-rod shadow patterns as well as the zero-rod distribution. For better comparison they were normalized to satisfy $S(y=0)=1$. The solid curves are the corresponding shadows calculated from the downstream model discussed above. We found that the Lorentzian scattering kernel matched the experimental data a little bit better than the Gaussian form for these particular scattering parameters and arrangements of rods. This agreement is certainly not perfect and different scattering kernels could improve the match. The five theoretical curves were fitted with a single free parameter δ_S=0.53. The set for $S_{0001}(y)$ corresponds to the case where the absorber is closest to the laser source. It has the widest shadow, confirming that shadows can widen in a scattering medium as predicted by the downstream model.

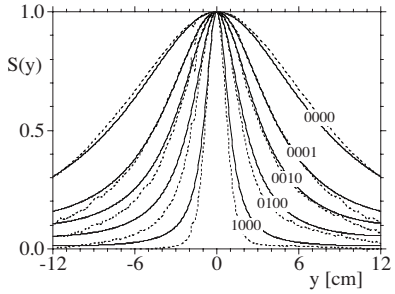

FIG. 3. Experimental shadow functions $S_{0000}(y)$, $S_{1000}(y)$, $S_{0100}(y)$, $S_{0010}(y)$, and $S_{0001}(y)$. The graphs were normalized to $S(y=0)=1$. The scattering medium was a mixture of 100 ml of 2% milk with 9.2 liters of water and the rods were at locations z_1 =6.5 cm, z_2=8.8 cm, z_3=11.1 cm, and z_4=13.4 cm. For comparison, the dashed curves correspond to the corresponding data obtained from the downstream model with a Lorentzian scattering kernel, δ_S=0.53, O_A=1, and incoming beam width w_L=0.11 cm.

IV. DECOMPOSITION BASED IMAGING (DBI)

For our DBI scheme, the four single-rod shadow patterns S_{0001}, S_{0010}, S_{0100}, and S_{1000} form the calibration states. For brevity, we denote these four states by $V_n(y)$, with n =1,…,4. The goal in the DBI method is to express each of the eleven multirod shadow patterns approximately as an arithmetic sum of the four calibration states with optimum weight factors λ_n. The states $V_n(y)$ are typically positive and not orthogonal to each other. As a result, a quantum mechanical-like decomposition scheme based on simple scalar products does not work. The decomposition was done by using the standard χ^2 linear least square fitting approach [14], where the factors λ_n were determined from minimizing the error between the particular shadow signal $S_{ijkl}(y)$ and the superposition of the calibration states

$$\chi^2\{\lambda_n\} \equiv \int dy \left[S_{ijkl}(y) - \sum_{n=1}^{n} \lambda_n V_n(y) \right]^2 f(y)^2. \quad (4.1)$$

The arbitrary function $f(y)$ can be used to give certain spatial regions in y more weight; for example, it could be chosen proportional to the volume element in 3D. For simplicity we chose $f(y)=1$. The resulting four linear equations for the weights λ_n can be obtained from the four conditions $\partial\chi^2/\partial\lambda_n=0$. The four weights λ_n are obtained by a simple matrix inversion.

In Table I(a) we show the resulting weight factors λ_n for the experimental data. For a better comparison, the digits in the parentheses indicate the presence (1) or absence (0) of an absorber. We note that some configurations require negative weights or weights with absolute values larger than unity in order to approximate the image obtained from the multiple absorbers. For example, the two-absorber shadow $S_{1100}(y)$ [first row of Table I(a)] requires λ_2=−0.342 and λ_1=0.162, even though there were no absorbers at z_2 and z_1 in this particular configuration.

TABLE I. The weight factors λ_1, λ_2, λ_3, and λ_4 associated with the shadow basis states S_{0001}, S_{0010}, S_{0100}, and S_{1000} for eleven different absorber combinations. The presence or absence of an absorber is indicated by the number in parentheses. (a) Experimental data for the four-rod system described in Sec. III. (b) Theoretical data: Scattering strength $\delta_S=0.53$, absorber diameter $d=0.95$ cm, $O_A=1$, and incoming laser width $w=1.1$ cm.

(a) Weight factors for the experimental data

λ_4	λ_3	λ_2	λ_1
0.682(1)	1.156(1)	−0.342(0)	0.162(0)
0.827(1)	0.136(0)	0.635(1)	0.176(0)
0.793(1)	0.112(0)	−0.152(0)	1.051(1)
−0.015(0)	0.680(1)	0.961(1)	0.036(0)
−0.007(0)	0.795(1)	−0.109(0)	1.072(1)
−0.004(0)	0.070(0)	0.294(1)	1.220(1)
0.591(1)	0.556(1)	1.505(1)	−0.391(0)
0.564(1)	0.641(1)	0.348(0)	0.859(1)
0.706(1)	−0.042(0)	0.606(1)	1.072(1)
0.015(0)	0.297(1)	1.016(1)	0.919(1)
0.556(1)	0.138(1)	1.571(1)	0.502(1)

(b) Weight factors for the theoretical signals with noise

λ_4	λ_3	λ_2	λ_1
0.679(1)	1.173(1)	−0.203(0)	0.074(0)
0.832(1)	−0.105(0)	1.169(1)	−0.072(0)
0.880(1)	−0.193(0)	0.292(0)	0.880(1)
0.039(0)	0.439(1)	1.425(1)	−0.173(0)
0.017(0)	0.732(1)	0.077(0)	0.974(1)
0.004(0)	0.021(0)	0.647(1)	1.027(1)
0.574(1)	0.938(1)	0.723(1)	0.104(0)
0.556(1)	1.140(1)	−0.497(0)	1.202(1)
0.719(1)	−0.189(0)	1.069(1)	0.830(1)
−0.055(0)	0.837(1)	0.395(1)	1.115(1)
0.554(1)	0.677(1)	0.547(1)	1.066(1)

Even though the associated value of χ^2 can be computed for each run and it is a measure of how well the optimum superposition of the calibration states matches the multirod image, it is not clear whether it should be used as a direct indicator of the quality of the particular reconstruction. As the calibration states are nonorthogonal, the best-fit superposition with a very small value of χ^2 could be obtained from "incorrect" weight factors λ_n that do not represent the true presence or absence of the rods. On the other hand, a large value of χ^2 could be associated with weight factors that represent the actual rods more accurately than for smaller χ^2.

In order to have a less ambiguous measure for the accuracy of the reconstruction scheme we introduce a new quantity. It is based on the assumption that a calibration state associated with a rod that is absent in the multirod configuration should have ideally a vanishing weight in the superposition. In our signal space of eleven multirod configurations with a total of 44 weights factors, 16 weights correspond to an absent rod indicated by (0). We therefore define a contamination factor C as the average of the (absolute value) of all those 16 weight factors that correspond to an absent rod. For our experimental data in Table I(a), this amounts to $C=0.13$. This value is sufficiently close enough to zero that the identification of the nonexistent rods should be possible.

In order to examine how this factor C depends on various parameters such as the scattering strength δ_S, the absorbers' opacity O_A, and also on noise, we have used the downstream model to generate the eleven multirod configurations. The simple structure of the downstream model indicates that C depends only on the ratio d/δ_S. In other words, doubling the absorbers' diameter leads to the same result as halving the scattering strengths.

From the simulations for the experimentally suggested parameters $\delta_S=0.53$, $w_L=0.11$ cm, $d=0.96$ cm, $O_A=1$, $W=16$ cm, and no noise we have obtained a contamination factor $C=0.0025$. This remarkably small value suggests that it is the experimentally unavoidable noise that deteriorates the inversion quality. At least in principle, the simple analytical structure of the downstream model could also predict scattering profiles that are easier to invert than the experimental curves. But this is not very likely as simulations based on the Gaussian scattering kernel lead to similarly accurate inversions in the absence of noise.

In order to simulate this noise, we have multiplied each of the eleven signals $S_{ijkl}(y)$ with a factor $(1+r)$, where r denotes a uniformly distributed random number between $-R<r<R$ for each location y. It turns out that a noise level of $R=4.5\%$ increases the parameter C for the theoretical signals to the same value as for the experimental data, $C=0.13$. In Table I(b) we have shown all 44 weights for the theoretical data with a multiplicative noise of 4.5%. Even though the noise makes a direct comparison of experimental with theoretical weight factors less meaningful, there are still common trends. For example, the state (0011) seems to be quite robust under noise whereas the weights for (1101) deteriorate significantly. The theoretical data also reveal a simple scaling law for a small level of noise; we found that on average for $0.5\%<R$ the contamination factor scales linearly with R. For a noise level R exceeding about 25%, the factor C exceeds 0.5, making the decomposition based method very unreliable. In separate simulations we have also included additive noise and found that similar conclusions about the qualitative behavior of C hold.

In the series of Figs. 4 we show how the accuracy of DBI depends on various parameters. In Fig. 4(a) we display C as a function of the inverse scattering strength δ_S^{-1}. We see that independent of the absorber's size d, a higher scattering (low δ_S^{-1}) increases the accuracy of our scheme. This particular scaling in our approach to imaging is extremely helpful as a large level of scattering makes a practical imaging in turbid media usually more difficult. We note, however, that in the limit of very large scattering certain analytical approximations to the forward model, such as the diffusion theory, become applicable that can simplify the theoretical framework for the inversion. This limit might also suggest a better form for the scattering kernels.

For comparison, we have also included by the dashed line the difference between the true shadow and their best possible fit as defined in Eq. (4.1). The parameter $\chi^2(\delta_S^{-1})$ shows

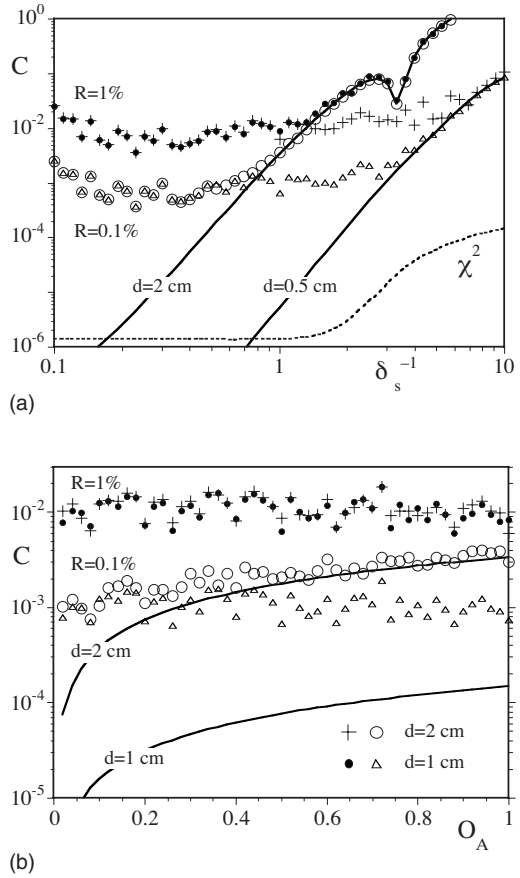

FIG. 4. (a) Average contamination factor C for the eleven multiabsorber configurations as a function of the inverse scattering parameter δ_S^{-1}. The symbols represent various levels of multiplicative noise in the signals. The dashed line is the least square fitting parameter χ^2 for $d=2$ cm and $R=1\%$. All data are computed from the downstream model with the same parameters as in Fig. 2. (b) Average contamination factor C as a function of the opacity O_A of the absorbers.

usually the same qualitative trends as the contamination factor $C(\delta_S^{-1})$. As δ_S^{-1} decreases from $\delta_S=10$ to 0.1, χ^2 changes from 0.18 to much smaller values that depend on the amount of noise R. The lower values at $\delta_S^{-1}=0.1$ are $\chi^2=10^{-8}$ (for $R=0$), $\chi^2=6\times10^{-3}$ (for $R=0.1\%$), and $\chi^2=6\times10^{-2}$ (for $R=1\%$). This behavior of χ^2 would (incorrectly) suggest a monotonic deterioration of the method with increasing δ_S^{-1}. However, the contamination graph for $d=2$ cm shows that this trend is not monotonic; in fact, with $C(\delta_S=3.3)=0.03$ the DBI method works better than for larger $[C(\delta_S^{-1}=2.75)=0.08]$ as well as for smaller amounts of scattering $[C(\delta_S^{-1}=4)=0.2]$. As seen from the monotonic graph for $\chi^2(\delta_S^{-1})$, this island of increased accuracy would not have been identified based on χ^2. As χ^2 is the result of an averaging over a much larger number of fluctuating quantities, it also fluctuates much less than C.

Unfortunately, small levels of multiplicative noise deteriorate the accuracy of DBI significantly. For $R=0.1\%$ the lowest possible contamination is about $C=0.001$ and for $R=1\%$ it grows to $C=0.01$. We purposely chose identical sequences of random numbers for the computations to show two aspects. First, we see that for sufficiently large scattering $(1<\delta_S)$ the contamination factors become independent of the absorber's size d for the same noise level R. Second, as we decrease the noise level from $R=1\%$ to 0.1%, the corresponding contamination shrinks precisely by a factor of 10 suggesting a linear scaling of C as a function of R. An unacceptable value of $C>0.5$ would be reached at the 10–30 % noise level, independent of the size of the absorber.

The nearly constant value of $C(\delta_S)$ for nonzero noise and for sufficiently large scattering can be understood as the result of a cancellation of two competing mechanisms. The underlying noise-free contamination C decreases nearly like a power law $C\sim\delta_S^{-m}$ making DBI more accurate for $\delta_S\to\infty$. In the same high-scattering limit, however, the resulting shadow patterns for various rod configurations become also more similar to each other which makes it easier for the noise to wash out their relative differences. Once the data for different rod configurations become too similar, DBI has to fail suggesting the opposite trend of an increasing C for $\delta_S\to\infty$.

In Fig. 4(b) we show that the contamination decreases with increasing opacity O_A of the absorbers. With respect to a practical imaging device, this trend is again favorable as a real obstacle in a biological tissue, e.g., usually partially transmits the light and does not necessarily have 100% opacity as the plastic rods we used in our experiment. Similar to Fig. 4(a) any noise will deteriorate the image quality; this is especially significant for absorbers with small physical extension as seen by the graph for $d=1$ cm for $R=0\%$, 0.1%, and 1%. For a larger rod diameter and large opacity, the contamination factor is similar for no noise and $R=0.1\%$. For larger levels of noise $(R>1\%)$, the contamination is nearly independent of the opacity as well as the diameter. This can be seen by the two almost flat curves at the top of the figure.

V. RESOLUTION IMPROVING ALGORITHM

In our experiment [Table I(a)] the largest weight associated with a nonexistent rod is 0.348 (in 1101), whereas the smallest weight that is associated with an existing rod is 0.294 (in 0011). This means that a simple algorithm that changes globally the weight factors to either 0 or 1 based on a given threshold value would not work for our data. This failure is simply a consequence of the fact that absorbers that are in the shadow of other absorbers cannot obtain enough light to contribute to the shadow strength. As an example, the leftmost absorber in (1111) has only a weight factor of 0.556 for the calibration state S_{1000} that was obtained under an unblocked illumination.

Below we propose an algorithm that can improve the weights subsequently. It is based on the observation that the weights λ_1 that are associated with a vanishing rod at z_1 are easiest to identify. For example, in all eleven signal runs, the largest value of these weights is only 0.176 (in 1010). Once we have identified an (in principle) vanishing weight, we can omit the particular calibration state $V_1(y)$ and minimize the shadow pattern again with respect to the remaining three states V_4, V_3, and V_2. As the four original weights of all

modes are directly coupled, the other weights might become also difficult to interpret. If we take the run (1100) as an example, the rematching with three states changes the four weights from [0.682 (1), 1.156 (1), −0.342 (0), 0.162 (0)] to [0.701 (1), 0.992 (1), −0.004 (0), 0 (0)]. This is obviously a significant improvement as now (in contrast to its previous value $\lambda_2=-0.342$) also the second weight λ_2 (=−0.004) can be uniquely identified as an absent rod. This scheme can be repeatedly applied for all runs in which a weight is sufficiently small to suggest an absent rod.

In a similar fashion we can also clean up the data if the first weight λ_1 can be unambiguously identified with an existing rod. For example, the first weight λ_1 in the 1001 run (third row of the table) is 1.051. In this case we can subtract the corresponding identified calibration state from the signal, $S_{\text{new}}(y) \equiv S_{1001}(y) - 1$. $S_{0001}(y)$ and rematch the new data S_{new} without the state V_1. In this case the old set [0.793 (1), 0.112 (0), −0.152 (0), 1.051 (1)] changes to [0.800 (1), 0.049 (0), −0.033 (0)]. Once again the small second and third weights are significantly improved. Because of the linearity it is important that the state V_1 is removed with the weight 1. If we had used a weight factor of 1.051, the weights in the new superposition would be unaffected due to the linearity of our decomposition scheme.

VI. RESOLUTION FOR OFF-GRID ROD LOCATIONS

So far we have assumed that the possible locations of the rods in the signal space were restricted to the same locations as the rods of the calibration data. Let us now weaken this constraint and permit the rods to take arbitrary positions. Our method remains applicable to this more general situation if the shadow pattern of a rod that has been placed at location z between two grid points $z_{n-1} < z < z_n$ excites mainly the corresponding calibration states associated with the nearby neighbor grid locations, $V_{n-1}(y)$ and $V_n(y)$. If, however, it turns out that calibration states associated with locations further away are required as well in the optimum superposition, the corresponding weights cannot be used to identify unambiguously the position of the rods. Furthermore, if the associated neighboring signal states are the only states that lead to appreciable weights, then one could even use these two weights λ_n and λ_{n-1} to improve the resolution and attempt to reconstruct the precise rod location z.

To obtain some first insight into this question, we have increased our calibration space to nine [$V_n(y)$ where $n=1,\ldots,9$] associated with rods that are located at positions $z_n=1,2,\ldots,9$ cm inside a tank that extends from $z=0$ to $W=10$ cm. For simplicity, we have used a single test rod whose location z was varied continuously from 0 to 10 cm. For each location z we have computed the corresponding shadow pattern and decomposed it in the nine-dimensional calibration space. For rod positions z (<1 cm or >9 cm) that are not between two calibration points, the decomposition requires weights that are much larger than plus or minus unity, so the scheme fails for exterior positions. For locations z that are inside the calibration grid, the situation is fortunately much more favorable.

In Fig. 5 we show the corresponding five weights λ_n associated with the five calibration states V_2, V_3, V_4, V_5, and V_6

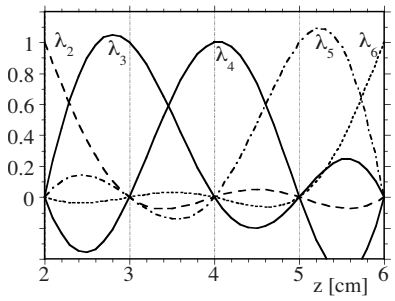

FIG. 5. Weight functions as a function of the location z of an absorber based on nine calibration states associated with locations $z=1,2,\ldots,9$ cm. ($\delta_S=0.34$, $d=0.95$ cm, $O_A=1$, $W=10$ cm, and $w_L=0.11$ cm.)

as a function of the single-rod position z. If this location z happens to match a particular grid point z_N, for consistency we have $\lambda_n=\delta_{n,N}$ forcing all weight states to vanish except one. The data are encouraging and suggest that the decomposition based method works nicely even for off-grid locations z. In the entire range 2 cm$<z<$6 cm the dominant weights are associated with the two direct neighbor modes. The largest deviation occurs for $z\approx 5.6$ cm, where the neighboring modes have the weights $\lambda_5\approx 0.85$ and $\lambda_6\approx 0.48$, respectively, but the mode V_3 contributes with a weight as large as $\lambda_3\approx 0.25$. In our experience, negative weights are usually associated with absent rods, so the negative weights do not disturb our decomposition scheme and can be eliminated by our algorithm of Sec. V.

We also notice some overshooting. In other words, the weights do not necessarily take their largest value at that value of z at which its corresponding calibration rod was centered. For example, the maxima are $\lambda_3\approx 1.05$ ($z=2.8$ cm), $\lambda_4\approx 1.0$ ($z=4$ cm), $\lambda_5\approx 1.09$ ($z=5.2$ cm), and $\lambda_6\approx 1.3$ ($z=6.4$ cm). This is related to the fact that all weights are coupled and if some turn negative, the other weights can increase beyond unity to compensate. This effect certainly makes the reconstruction of the rod location more difficult.

The weights are not perfectly symmetric between the corresponding grid locations. However, once the corresponding neighbor grid points are uniquely identified, one could use a linear approximation to model their z dependence. For example, we could assume that for 3 cm$<z<$4 cm the weights are approximated by $\lambda_3(z)\approx 1-(z-3)$ and $\lambda_4(z)\approx 1+(z-4)$. If we invert this simple formula to predict the location z as a function of the two weights, we obtain $z_3(\lambda_3)\approx 4-\lambda_3$ and $z_4(\lambda_4)\approx \lambda_4+3$. As the predicted positions are systematically overestimated and underestimated by the two weights, respectively, we can take the average value, $Z_{\text{pred}}(\lambda_3,\lambda_4)\equiv(7-\lambda_3+\lambda_4)/2$, as the predicted position of the rod. To examine the accuracy of this estimate, we have graphed in Fig. 6 the relative error, defined as $|Z_{\text{pred}}-z|/z$ as a function of the true position z. As expected the error is zero close to the grid points $z=3$ and 4 cm. In the entire interval, the largest error is less than 2% amounting to an uncertainty of less than 1 mm. In other words, finding the predicted location of the rod by interpolating the corresponding neighboring weight factors permits the scheme to increase its predicted accuracy far beyond the spatial scale given by the grid

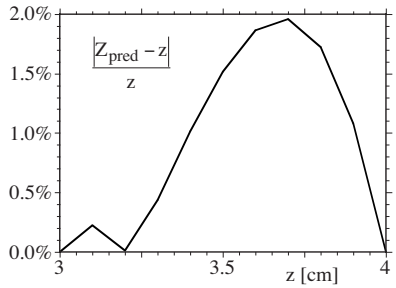

FIG. 6. Relative error between the predicted position Z_{pred} of the rod according to the weight factors λ_3 and λ_4 as a function of z. The two weights are obtained from Fig. 5.

point spacing of the calibration runs. We note that this scheme for off-grid rods as well as the resolution improving algorithm discussed in the previous section require that the rods are identical to those used for the calibration runs. For the more general case in which the size or optical properties of the rod configurations differ from those used in the single-rod calibration measurements, more systematic studies are required to determine the direct practical applicability for bio-optical systems.

VII. SUMMARY AND CONCLUSION

We have examined the range of applicability of the decomposition based imaging method [25]. In contrast to most imaging techniques, DBI requires the *a priori* calibration of the medium. This calibration is accomplished by placing a representative single absorber into the medium at various locations and measuring the resulting scattered light spectrum outside the medium. DBI is based on an *ad hoc* assumption that the resulting shadow patterns in the scattered light associated with several absorbers can be related to a simple superposition of shadow patterns associated with each absorber separately. As this equality is valid only approximately, we had to use a multiregression analysis to determine the best-fit weights for each single-absorber shadow pattern instead of a direct inversion. Also, in contrast to the usual Born or Rytov approximation of diffusive imaging, which permits a mathematical derivation of the corresponding Fredholm integral equation, a similar derivation for DBI is presently lacking. As a consequence, it is nontrivial to evaluate analytically the region of validity of DBI and it therefore requires a numerical analysis of the final data. We introduced the contamination parameter C as quantitative measure of the accuracy of the reconstruction method for all possible rod configurations.

Using this measure we could show systematically that DBI works best for large scattering media and absorbers with small extension. For multiplicative noise, the accuracy of the method becomes independent of the diameter and the scattering strength of the background medium. We also proposed an algorithm that can improve the position reconstruction from our experimental data significantly. Furthermore, we suggested that if an object is placed at a location that has not been previously recorded for a prior single absorber, mainly the nearby single-absorber modes are important. These weight factors can be used to interpolate the precise location of the absorber with surprising accuracy.

The present work examined absorbers that were arranged along the beam line to study the impact of the mutual blocking of the light. In order to generalize DBI to a fully two- or three-dimensional scheme, we have to understand how DBI works if absorbers are placed along the transverse beam direction. Clearly, in the case the shadow patterns do not overlap, a unique decomposition of multiabsorber shadow patterns into single-absorber shadows can be done exactly. However, it is presently not clear how the scheme will work if the shadow patterns overlap.

ACKNOWLEDGMENTS

This work has been supported by the NSF. We thank P. Yu (U. Missouri, Columbia) for the loan of a special fiber and very valuable discussions. We also acknowledge support from BLV and Research Corporation for Cottrell Science Awards.

[1] S. Chandrasekar, *Radiative Transfer* (University Clarendon Press, Oxford, 1950).
[2] A. Ishimaru, *Wave Propagation and Scattering in Random Media* (Academic, New York, 1978), Vols. 1 and 2.
[3] E. P. Zege, A. P. Ivanov, and I. L. Katsev, *Image Transfer though a Scattering Medium* (Springer-Verlag, Berlin, 1991).
[4] G. M. L. Gladwell, *Inverse Problems in Scattering* (Kluwer Academic Publishers, Dordrecht, 1993).
[5] V. V. Tuchin, Phys. Usp. **40**, 495 (1997).
[6] O. Dorn, Inverse Probl. **14**, 1107 (1998).
[7] See Opt. Express **4**, 8 (1999), special issue on diffusive imaging.
[8] *The Essential Physics of Medical Imaging*, 2nd ed., edited by J. T. Bushberg, J. A. Seibert, E. M. Leidholdt, Jr., and J. M. Boone (Lippincott William & Wilkins, Philadelphia, 2002).
[9] S. R. Arridge, Inverse Probl. **15**, R41 (1999).
[10] K. Wood, D. Smith, B. Whitney, K. Stassun, S. J. Kenyon, M. J. Wolff, and K. S. Bjorkman, Astrophys. J. **561**, 299 (2001).
[11] S. Rost and J. Revenaugh, Science **294**, 1911 (2001).
[12] V. A. Ermolchev and M. L. Zaferman, J. Mar. Sci. Technol. **60**, 544 (2003).
[13] M. Röhriga, H. Stützela, and C. Alta, Agron. J. **91**, 1024 (1999).
[14] See, e.g., R. C. Aster, B. Borchers, and C. H. Thurber, *Parameter Estimation and Inverse Problems* (Elsevier Academic Press, Amsterdam, 2005).
[15] P. M. Morse and H. Feshbach, *Methods of Theoretical Physics, Part I & Part II* (McGraw-Hill, New York, 1953).
[16] G. B. Arfken and H. J. Weber, *Mathematical Methods for Physicists*, 6th ed. (Elsevier, Amsterdam, 2005).

[17] For more detailed accounts of the Born approximation, see D. A. Boas, Ph.D. thesis, University of Pennsylvania, 1996, and M. A. O'Leary, Ph.D. thesis, University of Pennsylvania, 1996.
[18] M. A. O'Leary, D. A. Boas, B. Chance, and A. G. Yodh, Opt. Lett. **21**, 158 (1996).
[19] V. Ntziachristos and R. Weissleder, Opt. Lett. **26**, 893 (2001).
[20] E. E. Graves, J. Ripoll, R. Weissleder, and V. Ntziachristos, Med. Phys. **30**, 901 (2003).
[21] For a recent review on the Born approximation in fluorescence diffuse tomography, see A. Corlu, R. Choe, T. Durduran, M. A. Rosen, M. Schweiger, S. R. Arridge, M. D. Schnall, and A. G. Yodh, Opt. Express **15**, 6696 (2007), and many references therein.
[22] R. Weissleder and V. Ntziachristos, Nature (London) **9**, 123 (2003).
[23] E. M. C. Hillman, Ph.D. thesis, University College London, 2002.
[24] A. Li, G. Boverman, Y. Zhang, D. Brooks, E. L. Miller, M. E. Kilmer, Q. Zhang, E. M. C. Hillmark, and D. A. Boas, Appl. Opt. **44**, 1948 (2005).
[25] S. D. Campbell, I. L. Goodin, S. D. Grobe, Q. Su, and R. Grobe, Phys. Rev. A **76**, 063802 (2007).
[26] S. Campbell, S. Menon, Q. Su, G. H. Rutherford, and R. Grobe, Laser Phys. **17**, 117 (2007).
[27] S. D. Campbell, A. K. O'Connell, S. Menon, Q. Su, and R. Grobe, Phys. Rev. E **74**, 061909 (2006).
[28] S. Campbell, A. D. O'Connell, G. H. Rutherford, and R. Grobe, Opt. Lett. **32**, 560 (2007).